A Pharmacokinetic and Pharmacodynamic Model of an IL-12 Anchored-Drug Conjugate for the Treatment of Solid Tumors

Hitesh B. Mistry[1], David Hodson[1], Sailaja Battula[2], Michael M. Schmidt[2], Robert Tighe[2], Howard L. Kaufman[2], and Christophe Chassagnole[1]

ABSTRACT

IL-12 mediates innate and adaptive immune responses and has demonstrated therapeutic antitumor activity, but clinical development has been hindered by a narrow therapeutic window. We generated a novel IL-12–anchored drug conjugate by physiochemical linking of murine IL-12 to aluminum hydroxide (alum). The complex was designed to utilize alum as a scaffolding for durable retention of IL-12 within the tumor microenvironment as a strategy to increase the therapeutic window. To better define the systemic pharmacokinetic (PK) profile of the anchored IL-12 (mANK-101), a model-based assessment tool was developed to describe the systemic PK profile and downstream signaling factors following intratumoral injection of mANK-101. When compared with nonanchored IL-12, mANK-101 exhibited a distinct PK profile. Specifically, mANK-101 treatment was associated with a significant ninefold increase in the systemic terminal volume of distribution (Vd). Furthermore, linear mixed-effects models provided evidence that CD8^{+} T-cell infiltration and increased serum IFN-γ levels were correlated with tumor regression after a single dose of mANK-101. In addition, PK/pharmacodynamic modeling confirmed a link between systemic IL-12 and serum IFN-γ. The model also suggests that the anchored IL-12 drug conjugate is expected to prolong the absorption half-life (115 hours vs. 8 hours for the unanchored drug) with durable local retention and limited systemic absorption. In addition, serum IFN-γ may be a surrogate marker for drug activity. The PK modeling predictions may also contribute to determining the optimal clinical dose and schedule of mANK-101 and other anchored drug conjugates in patients with solid tumors.

Introduction

Immunotherapy has changed the clinical landscape for cancer treatment over the last decade. This is largely due to the therapeutic success of immune checkpoint blockade (ICB) in patients with solid tumors and chimeric antigen receptor (CAR) T-cell therapy in patients with hematologic malignancies (1, 2). Despite the success of ICB and CAR T-cell therapy, the majority of cancerous tumors exhibit innate or acquired resistance to treatment, and new therapeutic approaches are a high priority. One such approach involves immune agonist strategies, including cytokines like IL-12, which can stimulate a robust antitumor immune response. Despite its potential, systemic administration of IL-12 has been hampered by severe toxicity, limiting its clinical utility (3).

A promising approach to enhance the efficacy and therapeutic window of immune stimulators such as oncolytic viruses, Toll-like receptor agonists, cytokines, and mAbs is direct intratumoral delivery, aiming for prolonged local retention and limited systemic absorption. However, there are several barriers to effective drug retention within solid tumors, including high oncotic pressure, extensive neovascularization, stromal fibrosis, local hypoxia, and acidosis. Nonetheless, numerous agents, including cytokines, have been given locally with encouraging signs of therapeutic activity. Indeed, even local recombinant IL-12 was evaluated in patients with head and neck squamous cell carcinoma (4). In this study, recombinant IL-12 was rapidly absorbed into the systemic circulation, leading to dose-limiting toxicity (4).

To overcome some of the challenges associated with local drug delivery, we developed a novel platform for "anchoring" potent immune agonists, such as IL-12, directly within tumors using aluminum hydroxide (alum) as a scaffold (5). This approach is designed to promote longer retention within the tumor and result in lower diffusion into the systemic circulation. Although the precise duration of drug retention to be considered "anchored" has yet to be defined, there is emerging evidence that this approach has therapeutic activity at least in murine tumor models (5). Alum has a long history of safe use as a vaccine adjuvant, but recent data suggest that alum is generally inert and unlikely to have immune-adjuvant activity, although it possesses several desirable drug scaffold properties, including biocompatibility, biodegradability, and a high capacity for adsorbing payloads (6–8). To stably link IL-12 to alum, an aluminum-binding peptide (ABP) containing multiple serine phosphorylation sites was genetically fused to the cytokine, creating an IL-12–ABP protein. When admixed with alum, stable physiochemical linkage occurs through ligand exchange reactions between the phosphates on the ABP and the surface hydroxide groups of alum (5).

Preclinical studies have shown that alum-anchored murine IL-12 (mIL-12)–ABP (designated mANK-101) retains its pharmacologic activity within the tumor microenvironment, leading to enhanced antitumor activity in the absence of systemic toxicity in multiple tumor models (5, 9). In vivo, imaging demonstrated that up to 40% of the anchored IL-12 remains at the tumor site 21 days after injection (5). The IL-12–alum anchoring strategy has shown clinical

[1]Physiomics Plc, Abingdon, United Kingdom. [2]Ankyra Therapeutics, Cambridge, Massachusetts.

Corresponding Author: Christophe Chassagnole, Physiomics Plc, 140 Eastern Avenue, Milton Park, Abingdon OX14 4SB, United Kingdom. E-mail: cchassagnole@physiomics.co.uk

activity in dogs with melanoma in the absence of any dose-limiting toxicities (10).

Determining the pharmacokinetic/pharmacodynamic (PK/PD) relationships for intratumorally delivered anchored therapies presents unique challenges compared with traditional systemic administration. With efficiently retained intratumoral therapies, drug concentrations are expected to remain high at the injection site, with steep gradients extending into surrounding tissues, whereas systemic drug levels remain low. This spatial heterogeneity complicates the prediction of both therapeutic efficacy and systemic toxicity, as conventional plasma PK measurements do not accurately reflect the drug behavior within the tumor.

To address this challenge, we applied a quantitative pharmacology approach to mANK-101 using murine tumor model data. Quantitative pharmacology offers powerful and robust tools in drug development. One such tool is referred to as mixed-effects modeling, in which observed experimental data are fitted to a model structure within a mixed-effects framework that captures population mean parameter values, as well as the interindividual variability within the parameter estimates (11). Mixed-effects modeling is often applied both clinically and preclinically in order to validate drug mechanisms of action and identify candidate biomarkers correlated with tumor responses (12). It can also be used to fit population PK/PD models in order to assist in identifying the optimal dosing strategies (13).

In this study, using a model-based assessment, we delineated the systemic PK profile of mANK-101 following intratumoral injection, revealing a distinct PK profile compared with intratumorally administered nonanchored mIL-12–ABP. Furthermore, we present a model-based assessment of the mechanism of action and dosage/scheduling of mANK-101, emphasizing the potential of certain tumor-derived and peripheral biomarkers as efficacy surrogates, which could significantly contribute to determining the optimal clinical dose and schedule. These results provide valuable data for the design of future human clinical trials.

Materials and Methods

Cloning, protein expression, and alum complex

The cloning, protein expression, and purification of mIL-12–ABP and formation of the mANK-101–alum complex were described in detail previously (5). The mIL-12–ABP sequence was published in international publication number, WO 2022/235755 A2, sequence ID 21 (14).

Cell lines

Two female mouse cancer cell lines were used in the study. MC38 was obtained from BioVector, NTCC Inc. (RRID: CVCL_B288), CT26 was obtained from Shanghai Institutes for Biological Sciences (RRID: CVCL_7254), and the cell line authentication was performed by Crown Bioscience by analyzing their SNPs. Master and working cell banks were generated in up to nine passages. Prior to freezing the master cell banks, *Mycoplasma* testing was performed using MycoAlert Mycoplasma Detection Kit (Lonza Bioscience-LT07-318). Once thawed, tumor cells were maintained *in vitro* at 37°C in an atmosphere of 5% CO_2 in air and were used within five passages. *Mycoplasma* testing was done for the cells in culture before every *in vivo* experiment.

Mouse models

Six- to eight-week-old female C57BL/6 mice ($n = 10$ per group) were subcutaneously inoculated with MC38 cells (1×10^6 cells), and once the tumors reached an average volume of 99 mm^3, mice were treated with a single intratumoral injection of 5 μg mIL-12–ABP protein or 5 μg mANK-101 (5 μg mIL-12–ABP + 50 μg alum). Non–tumor-bearing C57BL/6 mice were subcutaneously treated with the same treatments either as free protein or complexed with alum.

BALB/c mice ($n = 15$) were injected with 5×10^5 CT26 murine colorectal cancer tumor cells in their right flank. Once the mean tumor size reached 79 mm^3, mice were randomized into treatment groups of either vehicle (Tris-buffered saline) or mANK-101.

Tumor volumes were measured three times per week using a caliper, and the volume was expressed in mm^3 using the formula $V = (L \times W \times W)/2$, where V is the tumor volume, L is the tumor length (the longest tumor dimension), and W is the tumor width (the longest tumor dimension perpendicular to L). Mice were euthanized when the tumor area exceeded 2,000 mm^3 or in the case of significant tumor ulceration or weight loss beyond 20%.

Serum PK measurements

Plasma samples were collected at 0.083, 0.25, 0.5, 1, 3, 6, 24, 48, 72, 120, 168, and 336 hours from MC38 tumor–bearing mice after single intratumoral injection and non–tumor-bearing C57BL/6 mice after subcutaneous administration of 5 μg mIL-12–ABP protein or 5 μg mANK-101 (5 μg mIL-12–ABP + 50 μg alum), with half of the animals in each group sampled at alternating time points. Plasma concentrations of mIL-12–ABP were determined at each time point using a Meso Scale Discovery V-PLEX Mouse IL-12p70 electro-chemiluminescence assay (Cat. #K152QVD-2), in accordance with the manufacturer's protocol adapted to use mIL-12–ABP as the standard curve. The range of detection for mIL-12–ABP was 30.86 pg/mL (lower limit of quantification) and 126,400 pg/mL (upper limit of quantification).

Comparative PK analysis of mIL-12–ABP and mANK-101

A comparative analysis of mIL-12–ABP and mANK-101 PK profiles after subcutaneous administration in tumor-naïve mice as well as intratumoral administration in mice challenged with the MC38 syngeneic tumor cell line was also performed. A PK model was fitted using the Levenberg–Marquardt algorithm in order to capture the effect of alum co-administration on mIL-12–ABP plasma exposure. The final PK model assumes that mIL-12–ABP plasma PK follows a biexponential distribution and is shown below:

$$\frac{dmIL12_{ABP[D]}}{dt} = -k_{a,1}mIL12_{ABP[D]}$$

$$\frac{dmIL12_{ABP[C]}}{dt} = k_{a,1}mIL12_{ABP[D]} - (k_{12} + k_e)mIL12_{ABP[C]} + k_{21}mIL12_{ABP[P]}$$

$$\frac{dmIL12_{ABP[P]}}{dt} = k_{12}mIL12_{ABP[C]} - k_{21}mIL12_{ABP[P]}$$

$$mIL12_{ABP[Conc]} = \frac{mIL12_{ABP[C]}}{\frac{V_1}{F}}$$

$$\frac{dmANK101_{[D]}}{dt} = -k_{a,2}mANK101_{[D]}$$

$$\frac{dmANK101_{[C]}}{dt} = k_{a,2}mANK101_{[D]} - (k_{12} + k_e)mANK101_{[C]} + k_{21}mANK101_{[P]}$$

$$\frac{dmANK101_P}{dt} = k_{12}mANK101_{[C]} - k_{21}mANK101_{[P]}$$

$$mANK101_{[Conc]} = \frac{mANK101_{[C]}}{\frac{V_2}{F}}$$

This model assumes that PK profiles follow the same distribution irrespective of the injection site. Variables $mIL12_{ABP[D]}$, $mIL12_{ABP[C]}$, and $mIL12_{ABP[P]}$ represent the amount of mIL-12–ABP in the extravascular depot, central compartment, and peripheral compartment, respectively. Variables $mANK101_{[D]}$, $mANK101_{[C]}$, and $mANK101_{[P]}$ represent the amount of mANK-101 in the extravascular depot, central compartment, and peripheral compartment, respectively. Parameters $k_{a,1}$ and $k_{a,2}$ reflect the absorption rate constants from the depot of mIL-12–ABP and mANK-101, respectively. Parameters k_{12} and k_{21} reflect the intercompartmental transition rates of mIL-12–ABP or mANK-101 between the central compartment and the peripheral compartment. The parameter k_e reflects the elimination rate of mIL-12–ABP or mANK-101 from the central compartment. $mIL12_{ABP[C]}$ and $mANK101_{[C]}$ are then scaled by their apparent volumes of distribution, which reflects the plasma concentration of mIL-12–ABP ($mIL12_{ABP[Conc]}$) or mANK-101 ($mANK101_{[Conc]}$). V_1/F represents the apparent terminal volume of distribution of mIL-12–ABP, and V_2/F represents the apparent terminal volume of distribution of mANK-101. Thus, in the context of this model, mIL-12–ABP and mANK-101 are assumed to share the same distribution and elimination rates from the central and peripheral compartments but are assumed to differ in their rates of absorption and volumes of distribution within the central compartment, in which any changes in their apparent volume of distribution are considered to be a direct consequence of changes in their bioavailability. The PK model schematic is shown in **Fig. 1**. The model assumes that the absorption rate and systemic bioavailability are different for mIL-12–ABP and mANK-101, but the systemic PK parameters k_e, k_{12}, and k_{21} are the same as we assume that we are measuring free mIL-12 in plasma.

Flow cytometry

Tumor, spleen, tumor-draining lymph node, and blood samples were harvested from CT26 tumor–bearing mice on the seventh day after treatment, processed as single-cell suspensions and analyzed by flow cytometry. Cells were blocked with 1 μg/mL Fc-Block (Mouse BD Fc Block Cat. #553141) and stained with a cocktail for surface antibodies (Supplementary Table S1) for 30 minutes at 4°C in the dark. Blood samples were treated with 2 mL of red blood cell lysing buffer (BioGems, Cat. # 64010-00-100) at 4°C for another 10 minutes in the dark. After washing, cells were fixed using fixation/permeabilization working solution for 30 minutes at room temperature in the dark. Following this, cells were permeabilized by washing twice in 1× permeabilization buffer (made from 10× permeabilization buffer, diluted with distilled H₂O). Cells were stained with intracellular antibodies for 30 minutes at room temperature in the dark. Finally, cells were washed twice and resuspended in FACS buffer for analysis on flow cytometer. A measure of 100 μL of 123count eBeads was added to each sample to calculate cell counts.

Cytokine analysis

Plasma was collected from CT26 tumor–bearing mice at various time points after intratumoral treatment of mANK-101 at different doses/schedules. Systemic IFN-γ levels were measured in plasma using mouse Meso Scale Discovery V-PLEX kit (Cat. #K152A0H-4), following the manufacturer's instructions. The calibration curves used to calculate IFN-γ concentration were

established by fitting the signals from the calibrator to a four-parameter logistic model.

Modeling

Three model-based analyses were performed to explore the relationship between biomarkers and efficacy. The first analysis focused on delineating the systemic PK profile of alum-anchored versus -unanchored IL-12–ABP following intratumoral injection. The second analysis was related to the short-term treatment effect after a single dose of mANK-101 and explored the correlation between immune cell infiltration biomarkers from excised tumors and tumor growth. The third analysis explored longer-term studies, which considered different schedules and measured potential plasma biomarkers and their correlation with efficacy.

Modeling strategy

Model-informed biomarker detection was used to confirm the statistical and biological significance of each candidate biomarker. Prior to model fitting, tumor volumes were scaled into radii after assuming a spherical geometry. As tumor radius has been shown to grow linearly with time (15), a linear mixed-effects model framework was incorporated to describe the rate of tumor growth over time in each treatment cohort. In order to confirm the significance of treatment effect on population tumor growth rates, comparison in model fits between a null model (model M1), which assumes no treatment effect, was performed alongside an extended model (model M2), which assumes that treatment significantly affects the tumor growth rate.

Statistical analysis and plotting

In the CT26 mouse model, data from a biomarker study were collected, which included paired tumor growth data and immune infiltrate biomarker data. The biomarker study collected three timepoints of tumor growth data before each animal was sacrificed for generation of the immune infiltrate data.

These data were analyzed in the following way using nested linear mixed-effects models and the likelihood ratio test (LRT) as we described below.

Tumor volumes were mapped onto a sphere, and the value was converted to radius; this allowed us to use linear models for analyses. The initial model fitted to the data assumed no treatment effect:

$$M1 : R_{ij} = R0 + g_i t_{ij} + e_{ij}$$

where the radius at time i for mouse j, R_{ij}, is equal to the initial radius value, $R0$, assumed to be the same for all mice; the growth rate for mouse j, g_i, assumed to be normally distributed with unknown mean and variance; and residual error, e_{ij}, which is the unexplained variance in the data and is assumed to be normally distributed with mean 0 and unknown variance.

M1 is then compared with a model that included a treatment effect parameter to confirm a treatment effect exists, as mentioned below.

$$M2 : R_{ij} = R0 + \left(g_i + d_1 mANK101_i\right) t_{ij} + e_{ij}$$

where d_1 is the treatment effect parameter describing the difference between control mice and those treated with mANK-101.

Having established the size of the treatment effect, the next step was to assess if the distribution of biomarker values on the final day

of tumor measurement showed a difference between control and treated animals. This was performed graphically by comparing the distribution of the markers across the treatment arms. Markers that showed a difference between control and treated groups were then taken forward into the following analyses.

M1 was compared with a model that includes a candidate biomarker to confirm if the biomarker explains any of the variance in growth rates:

$$M3: R_{ij} = R0 + \left(g_i + a_0 Biomarker_i\right) t_{ij} + e_{ij}$$

where $Biomarker_i$ is the biomarker value of mouse j, for each biomarker of interest and a_0 is the biomarker effect parameter. Next, to assess if the candidate biomarker fully captured the treatment effect, M3 was compared with the model below, which includes both biomarker and treatment:

$$M4: R_{ij} = R0 + \left(g_i + a_0 Biomarker_i + a_1 mANK101_i\right) t_{ij} + e_{ij}$$

where a_1 is the treatment effect parameter. If the addition of treatment effect did not improve model fit according to the LRT, then the biomarker is said to have fully captured the treatment effect and can be considered a surrogate for efficacy.

Plasma biomarkers

Data from longer-term CT26 mouse models in which different doses/schedules of mANK-101 were explored with respect to efficacy were collected. These studies also contained time-series data on serum IFN-γ, a marker of immune cell activation. Thus, a model linking injected dose of mANK-101 to serum IFN-γ and subsequently tumor growth inhibition was developed in the following way to assess if IFN-γ could be a potential noninvasive biomarker of efficacy.

A series of compartmental models were assessed to describe the kinetics of IFN-γ after administration of mANK-101. Based on graphical assessment of the data, a one-compartment model was considered the base model. This model was refined by incorporating a series of transit compartments to allow for flexibility in the rate of appearance of IFN-γ in plasma. The final model linking dose of mANK-101 to serum IFN-γ was

$$\frac{dmANK101}{dt} = -k_{a,1} mANK101$$

$$\frac{dT1}{dt} = k_{a,1} mANK101 - k_{a,1} T1$$

$$\frac{dT2}{dt} = k_{a,1} T1 - k_{a,2} T2$$

$$\frac{dIFNg}{dt} = k_{a,2} T2 - k_e IFNg$$

The first differential equation represents the compartment into which the dose of mANK-101 enters the system. The parameter ka,1 is a rate constant that represents numerous processes, which eventually leads to the production of IFN-γ in the tumors, T1 and T2, which is then released into plasma with rate constant $k_{a,2}$. The final differential equation represents the rate of change of IFN-γ in plasma, with ke representing the elimination of IFN-γ. This model was regressed against the IFN-γ kinetics observed in plasma after log-transforming the data from the study using the minpack.lm package in R.

After establishing a model linking injected mANK-101 dose and IFN-γ plasma kinetics, the next step involved using a classical

pharmacodynamic model, the indirect response model to represent the activation of the tumor killing immune system, I, as a function of IFN-γ plasma kinetics:

$$\frac{dI}{dt} = k_1 \left(1 + E_{max}\frac{IFNg^h}{EC50^h + IFNg^h}\right) - k_1 I$$

where k_1 is the turnover rate constant, E_{max} is the maximal increase in immune system–mediated tumor-cell killing, EC^{50} is the half-maximal concentration of IFN-γ observed in plasma, and h is the Hill coefficient. When $T2 = 0$ and $I = 1$, but we require that no immune system–mediated cell killing is present, thus we subtract 1 from $I(t)$ in the following equation, which describes the temporal evolution of tumor radius, R, over time:

$$\frac{dR}{dt} = g - (CD8 - 1)$$

where g is the growth rate of the tumor. The pair of differential equations, dI/dt and dR/dt, was regressed against the tumor size data, which was transformed to radius values by mapping the volumes onto a sphere.

Statistical analysis

All analyses were performed in R v 4.2.2 (RRID: SCR_001905), with the nlme package (RRID: SCR_015655) used for the immune infiltrate biomarker analysis and the minpack.lm package used for the plasma biomarker analysis and PK model fitting. The ggplot2 package was used for all visualization (RRID: SCR_014601). Statistical assessments of extended versus reduced models were performed by calculation of the $-2 \times$ log-likelihood ($-2LL$) followed by conduction of the LRT; LRT P values of less than 0.05 were deemed significant.

Data availability

The data used in this study are provided in the Supplementary Information for each figure with the corresponding plotting code.

Results

Comparative PK modeling of mIL-12–ABP and mANK-101

A PK model was fitted simultaneously to plasma PK profiles of mIL-12–ABP and mANK-101 in order to assess the impact of alum co-administration on systemic exposure to mIL-12–ABP. Parameter estimates are shown in Supplementary Table S2. All parameter estimates were deemed to be sufficiently precise as 95% confidence intervals were all within an acceptable range. Model fits indicated significant differences in the rate of absorption of mANK-101 compared with mIL-12–ABP and that absorption from the depot into the blood plasma is approximately 15 times faster without concurrent administration of alum, with an absorption half-life of approximately 8 hours for mIL-12–ABP compared with 115 hours for mANK-101. This indicates that the presence of alum is leading to prolonged retention of mIL-12–ABP in the extravascular region. In addition, the apparent volume of distribution (V/F) is approximately ninefold higher for mANK-101 when compared with V/F for mIL-12–ABP. This indicates a ninefold reduction in bioavailability from the extravascular region when mIL-12–ABP is co-administered with alum, further indicating that the mIL-12–ABP is more effectively retained within the injection site when co-administered with alum.

Figure 2 shows the model fit overlaid with the observed PK profiles of mIL-12–ABP and mANK-101 after subcutaneous
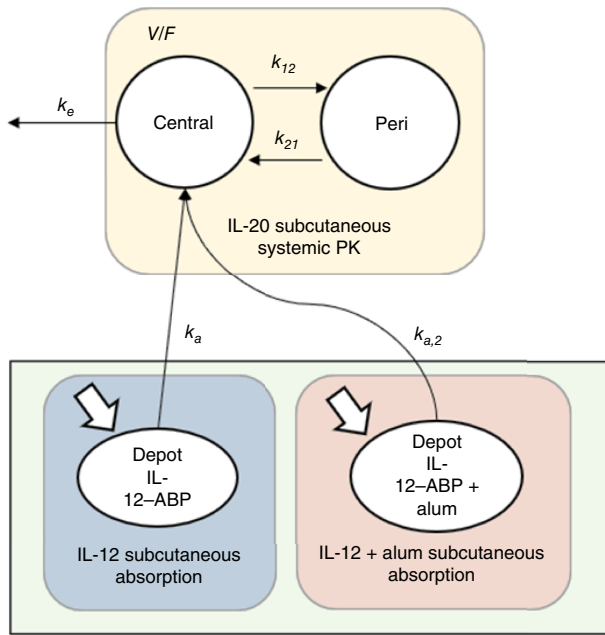
Figure 1.
Schematic of the final PK model for mIL-12–ABP and mIL-12–ABP + alum (mANK-101). Peri, peripheral.

injection in tumor-naïve C57BL/6 mice as well as after intra-tumoral injection in MC38 syngeneic tumors. Comparison of the model fits (black lines) with the observed PK profiles indicates reasonable concordance of the model fit to the data. The model exhibits an underestimation of the maximum concentration (Cmax) observed in the blood plasma when mANK-101 is administered intratumorally. However, incorporation of an additional parameter aiming to capture the higher Cmax observed in

the blood plasma during intratumoral administration did not lead to a significant reduction in the sum of square error value, measured via LRT and thus was not included in the final PK model.

Immune infiltrate biomarkers

The tumor growth inhibition data from the immune infiltrate study are shown in **Fig. 3A**. **Figure 3B** shows that the model M1 (red line) fits the data (blue dots) well. The comparison between M2 and M1 gave a P value of 0.002; that is, we can reject the null hypothesis that there is no treatment effect.

In the next step, we explored the biomarker data on the final day of tumor measurement (see **Fig. 4**). We can clearly see that certain biomarkers show a difference in distribution between the vehicle-treated and mANK-101–treated groups, for example, CD8 per CD45 and CD11b per PD-L1.

Next, we assessed how much of the variance in the growth rate can be explained by a single biomarker, that is, the difference between M3 and M1. The results of this analysis are shown in Supplementary Table S3. We can see that numerous markers ("%CV with biomarker" column) show a reduction in % coefficient of variation (%CV) when compared with the base model without biomarkers ("%CV base" column). Of all the markers, %CD8 explains most of the variance.

Next, to assess whether the top biomarkers highlighted in green in Supplementary Table S3 can fully capture the treatment effect, we compared M4 with M3. We found that inclusion of treatment did not improve model fit for CD8 per CD45 (M4 versus M3: $P = 0.795$) and CD11b per PD-L1 (M4 versus M3: $P = 0.579$). [Note that for CD8 per CD3, the treatment arm indicated improved model fit ($P = 0.018$), but the regression coefficient for the treatment arm was negative, suggesting that it is likely that CD8 per CD3 may overestimate antitumor effects rather than it not being related to antitumor effect.] As treatment effects cannot be estimated after including the markers, this suggests that these markers fully capture the treatment effect.

Figure 2.
PK model fits accurately reflect the observed plasma concentrations of mIL-12–ABP and mANK-101 after intratumoral injections in MC38 tumor–bearing mice and the subcutaneous injections in naïve non–tumor-bearing mice of the same genetic background (C57BL/6). Model fits (black lines) to tumor and tumor-naïve PK data (colored dots/lines) following a single administration. Solid colored dots and colored lines represent the mean concentration observed at each time bin, and shaded colored dots represent the observed data at each time bin ($N = 3$).
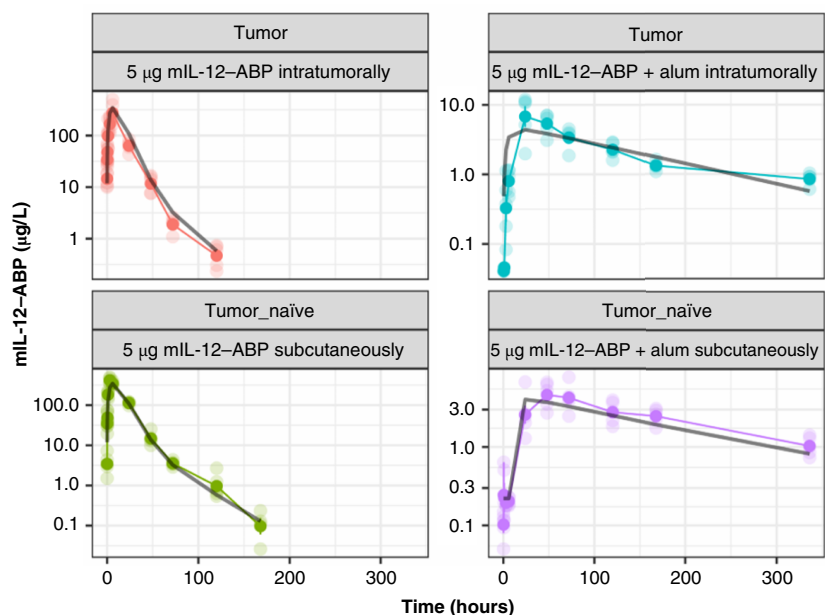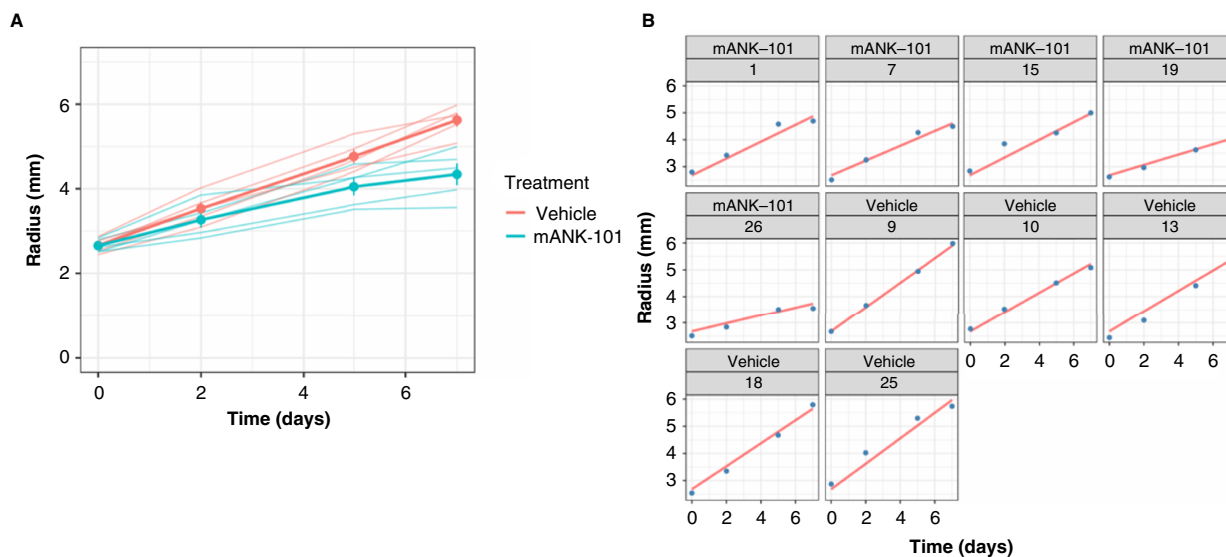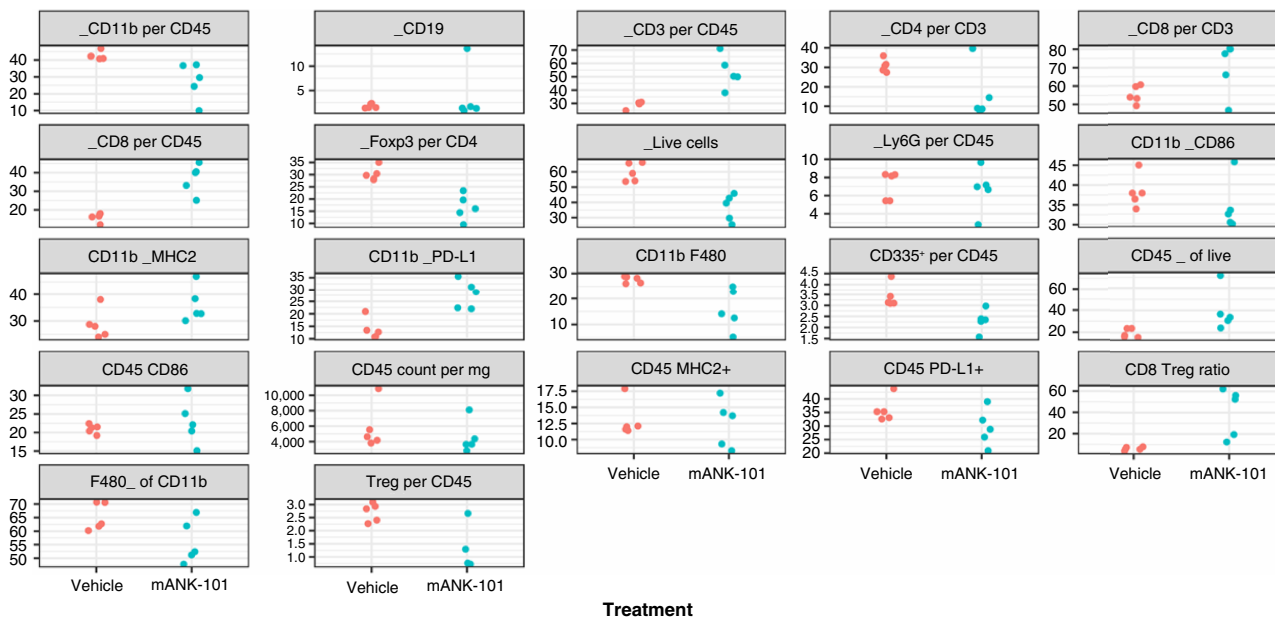
Figure 3.
mANK-101 reduces the tumor growth rate of CT26 tumors. **A,** Plot of the tumor growth data from the CT26 biomarker study—volumes converted to radius by mapping volumes onto a sphere. Faint lines are individual mice, darker lines represent the mean, and vertical lines represent the SD. **B,** Plot showing that model M1 fits (solid red line) to the raw tumor size data (blue dots) for the CT26 biomarker study.

Plasma biomarker

Model fits to the IFN-γ time series across the treatment arms can be seen in **Fig. 5**. The plots show that the structural model described in the "Materials and Methods" section captures the overall tendency of the data well. The biggest discrepancy between model and data is in the 5 μg, 7-day repeat study in which it seems that the IFN-γ levels may be decreasing over time, but there are dropouts in the data, which may well be skewing the mean. The final parameter values are shown in Supplementary Table S4.

Model fits to the tumor radius data over time using the derived IFN-γ model can be seen in **Fig. 6**. We see that the model describes the data well and that it correctly captures the repeat dosing of mANK-101, which reduces tumor escape. Furthermore, it indicates that low doses are likely to have a modest effect. These results

Figure 4.
Boxplots of key biomarkers assessed at day 7 indicate a role of CD8^{+} T-cell infiltration in mANK-101–mediated tumor control. Plots show the values of different immunophenotypic biomarkers between the control and mANK-101–treated CT26 tumors 7 days after treatment. Treg, regulatory T cells.
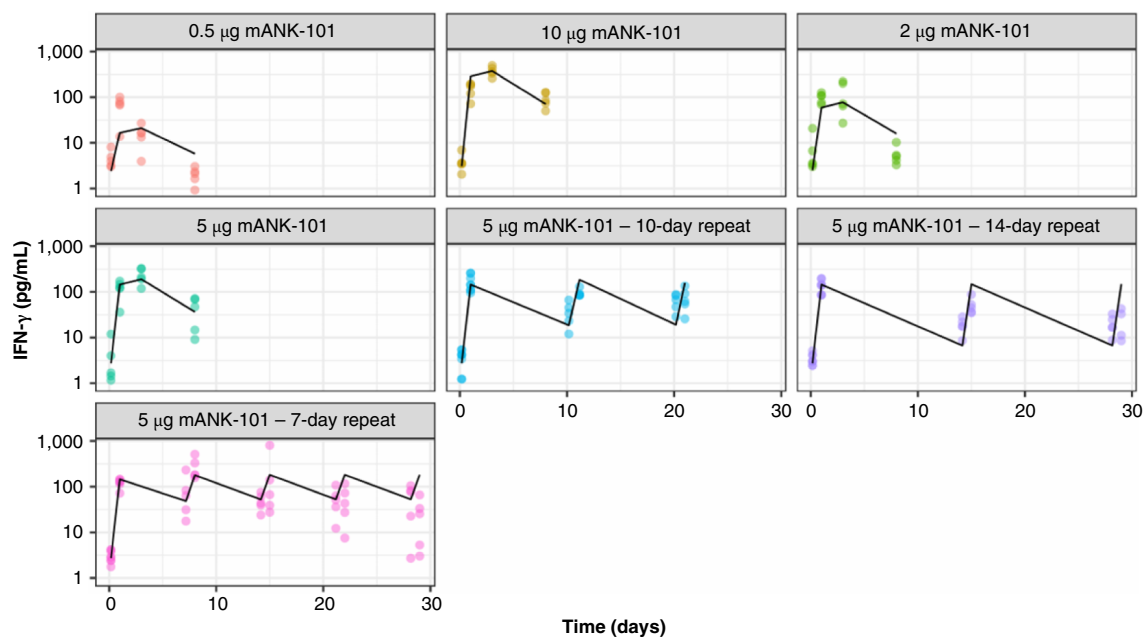
Figure 5.
Plot showing the model fit (thick gray line) to the observed IFN-γ time-series data (colored dots) for different doses/schedules of mANK-101 in the CT26 mouse model indicates that mANK-101 significantly increases IFN-γ concentrations within the blood.

suggest that plasma IFN-γ levels could be used as a surrogate for efficacy.

Discussion

Anchored drug conjugates can be generated by the use of alum as a biocompatible and biodegradable scaffold for intratumoral anchoring of anticancer therapies. Alum forms stable depots with a high payload capacity, making it ideally suited for sustained drug retention within established tumors. We have previously shown that an anchored IL-12 drug conjugate, mANK-101, takes advantage of this scaffold to induce potent antitumor immune responses while minimizing systemic toxicity (5). The unique retention properties of anchored drug conjugates require a sophisticated PK/PD modeling approach that integrates both intratumoral and peripheral biomarkers to correlate therapeutic responses with localized and systemic markers of immune activation.

Statistical confirmation of a biologically active drug capable of inducing local tumor control can be performed through various methods. The simplest method involves using parametric assessments of tumor size measured at different time points in order to assess whether the candidate drug reduces tumor size relative to a control. However, this method often contains insufficient resolution to confirm or deny particular effects of candidate biomarkers on tumor control and can only assess a limited number of data points, partially because an individual assessment of tumor sizes at a particular time point does not take into account the impact of a tumor's individual growth rate, as there are clear dependencies among the individual host, the time the tumor is the observed tumor diameter (16). Mixed-effects modeling provides a framework to statistically confirm whether a drug significantly affects the overall growth trajectory of the tumor and can utilize all data points in the process,

making it a much more powerful framework to determine effect sizes, which can then be used to assess correlations between biomarker values and effect size (12). In this study, we were able to confirm using mixed-effects modeling the significant dose-dependent treatment effect of mANK-101 on CT26 tumors, as well as the biomarkers that correlate most significantly with response.

Tumor growth data using the CT26 syngeneic model suggested a significant reduction in tumor growth rate by day 7, which was then captured when comparing model fit error values between a null model (M1) and treatment effect model (M2). Incorporation of a treatment effect reduced the -2LL value by 7 units, which indicates a strong reduction in error, clearly showing the significant impact of mANK-101 on the tumor growth rate with a single dose. CT26 tumors are always a good starting point to confirm the immune-stimulating effect of a particular treatment modality because of its high density of CD8$^+$ T cells (17). However, this immune-stimulating effect was also observed in B-16 tumors *in vivo* (5), which indicates that this treatment may be more effective in tumors with lower baseline levels of immune infiltrate (17).

Individual fits of tumor growth data confirmed that the Mayneord model of tumor growth (15) accurately captured the individual tumor growth trajectories at the time points assessed. It is important to use the most appropriate growth model when describing tumor growth in order to ensure that any correlations between growth rates and biomarkers are not affected by model specification errors (18). The zero-order growth rate of tumors has been understood mathematically since the 1930s (15), and the baseline tumor growth rate and drug-dependent changes in the tumor growth rate were accurately captured when incorporated into models M1 and M2, respectively. This provided a significant degree of confidence that any drug-dependent changes in biomarker values could be reliably estimated by assessing how different biomarker
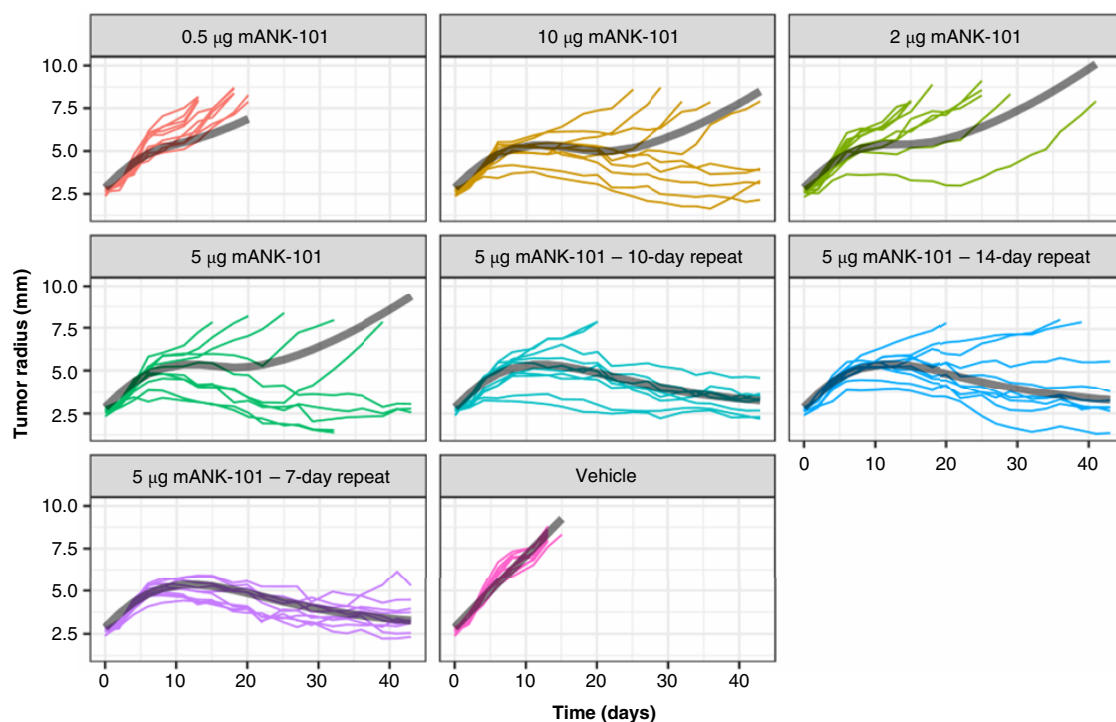
Figure 6.
Plot showing the model fit (thick gray line) to the observed tumor radius time-series data (colored lines represent each individual mouse) for different doses/schedules of mANK-101 in CT26 tumors confirms the dose-dependent impact of mANK-101 on tumor growth.

values could function as covariates affecting the random variability in tumor growth rates.

Model fits incorporating the effects of various biomarkers indicated that CD8+ T cells and PD-L1 expression levels significantly reduced the random variability in tumor growth rates by 50%. Although PD-L1 expression is considered immunosuppressive, PD-L1 levels are classic markers of a strong type-2 IFN-γ response (19). Thus, PD-L1 expression in this case is likely to be caused by stronger type-2 IFN-γ responses in the tumor, leading to increased T-cell proliferation and immunogenic cell death. This is further confirmed by prior data demonstrating increased T-cell proliferation following mANK-101 treatment (5). Further validation was suggested by biomarker estimates on the random variability in tumor growth rates (model M3) and the fact that further incorporation of a treatment effect (model M4) failed to further reduce -2LL values significantly. These data suggest that increased tumor PD-L1 expression could serve as a biomarker in the clinic to detect responses to IL-12–anchored drug conjugates, which is consistent with results from other immunotherapy modalities (19–21).

Although tumor biopsies provide a route to analyze changes in tumor microenvironment before and after treatment, tumor biopsies are also highly invasive (20). Liquid biopsies are becoming much more commonplace in health care due to the richer data that are available because of the relative ease of data acquisition, giving more opportunities for longitudinal assessments of tumor burden. In addition, advancing technologies are producing more robust assessments of biomarkers such as circulating tumor cells within the blood (21). PK/PD modeling describing drug-dependent changes in serum IFN-γ levels *in vivo* indicated a clear link between IL-12 exposure within the tumor and changes in IFN-γ levels. This

therefore provides potential avenue to assess this biomarker as a surrogate for responses when this drug is tested in the clinic. Furthermore, changes in serum IFN-γ levels could be used as a biomarker to infer optimal scheduling, by assessing when IFN-γ levels drop to baseline before administering an additional dose of mANK-101.

In summary, this work provides quantitative links between mANK-101 and its pharmacologic effects within the CT26 model. We found that CD8+ T cells significantly captured the initial treatment effect and that changes in PD-L1 expression and serum IFN-γ levels were biomarkers of therapeutic response to mANK-101. These results indicate further potential for combination effects with ICB and provide potential predictive biomarkers for immunologic and therapeutic responses, as well as aid in guiding drug dose selection and schedule. The modeling data will be confirmed in future clinical trials of IL-12–anchored drug conjugates in patients with advanced solid tumors.

Authors' Disclosures

Authors' Contributions

H.B. Mistry: Conceptualization, data curation, software, formal analysis, writing–original draft, writing–review and editing. **D. Hodson:** Validation, visualization, writing–original draft, writing–review and editing. **S. Battula:** Supervision, investigation, project administration, writing–review and editing. **M.M. Schmidt:** Conceptualization, supervision, writing–review and editing. **R. Tighe:** Supervision, project administration, writing–review and editing. **H.L. Kaufman:** Conceptualization, writing–review and editing. **C. Chassagnole:** Conceptualization, supervision, project administration, writing–review and editing.

Ethics Statement

All procedures involving the care and use of animals in the studies were performed according to the guidelines approved by the respective institutional animal care and use committees of Crown Bioscience and Wuxi AppTec, following the guidance of the Association for Assessment and Accreditation of Laboratory Animal Care International.

Acknowledgments

Note

References

1. Sun Y-J, Chen Y-C, Hua W-K, Wu SC-Y, Chan LL-Y. Comparison of chimeric antigen receptor-T cell-mediated cytotoxicity assays with suspension tumor cells using plate-based image cytometry method. Cytometry A 2023;103:27–38.

2. Mitra A, Barua A, Huang L, Ganguly S, Feng Q, He B. From bench to bedside: the history and progress of CAR T cell therapy. Front Immunol 2023;14:1188049.

3. Jia Z, Ragoonanan D, Mahadeo KM, Gill J, Gorlick R, Shpal E, et al. IL12 immune therapy clinical trial review: novel strategies for avoiding CRS-associated cytokines. Front Immunol 2022;13:952231.

4. van Herpen CM, Looman M, Zonneveld M, Scharenborg N, de Wilde PC, van de Locht L, et al. Intratumoral administration of recombinant human interleukin 12 in head and neck squamous cell carcinoma patients elicits a T-helper 1 profile in the locoregional lymph nodes. Clin Cancer Res 2004;10:2626–35.

5. Battula S, Papastoitsis G, Kaufman HL, Wittrup KD, Schmidt MM. Intratumoral aluminum hydroxide-anchored IL-12 drives potent antitumor activity by remodeling the tumor microenvironment. JCI Insight 2023;8:e168224.

6. Moni SS, Abdelwahab SI, Jabeen A, Elmobark ME, Aqaili D, Ghoal G, et al. Advancements in vaccine adjuvants: the journey from alum to nano formulations. Vaccines (Basel) 2023;11:1704.

7. Becker LC, Boyer I, Bergfeld WF, Belsito DV, Hill RA, Klaassen CD, et al. Safety assessment of alumina and aluminum hydroxide as used in cosmetics. Int J Toxicol 2016;35(Suppl 3):16S–33S.

8. He P, Zou Y, Hu Z. Advances in aluminum hydroxide-based adjuvant research and its mechanism. Hum Vaccin Immunother 2015;11:477–88.

9. Agarwal Y, Milling LE, Chang JYH, Santollani L, Sheen A, Lutz EA, et al. Intratumourally injected alum-tethered cytokines elicit potent and safer local and systemic anticancer immunity. Nat Biomed Eng 2022;6:129–43.

10. Barbosa MMP, Lopez AJ, Uyehara R, Kamerer RL, Schmidt M, Battula S, et al. Abstract 6347: preliminary results of an exploratory phase I clinical trial of anchored canine interleukin-12 (cANK-101) in dogs with advanced oral malignant melanoma. Cancer Res 2023;83(Suppl 7):6347.

11. Hodson D, Mistry H, Guzzetti S, Davies M, Staniszewska A, Farrington P, et al. Mixed effects modeling of radiotherapy in combination with immune checkpoint blockade or inhibitors of the DNA damage response pathway. CPT Pharmacomet Syst Pharmacol 2023;12:1640–52.

12. Hodson D, Mistry H, Yates J, Guzzetti S, Davies M, Aarons L, et al. Hierarchical cluster analysis and nonlinear mixed-effects modelling for candidate biomarker detection in preclinical models of cancer. Eur J Pharm Sci 2024;17: 106774.

13. Hodson D, Mistry H, Yates J, Farrington P, Staniszewska A, Guzzetti S, et al. Radiation in combination with immune checkpoint blockade and DNA damage response inhibitors in mice: dosage optimization via modelling and simulation. J Pharmacol Exp Ther 2023;387:44–54.

14. Schmidt MM, Zarbis-Papastoitsis G, Wittrup KD, Irvine D, inventor; Application filed by Danisco Us Inc., assignee. Fusion polypeptides. WO 2022/235755 A2. 2020 Sep 17.

15. Mayneord WV. On a law of growth of jensen's rat sarcoma. Am J Cancer 1932; 16:841–6.

16. Bell ML, Rabe BA. The mixed model for repeated measures for cluster randomized trials: a simulation study investigating bias and type I error with missing continuous data. Trials 2020;21:148.

17. Mosely SIS, Prime JE, Sainson RCA, Koopmann J-O, Wang DYQ, Greenawalt DM, et al. Rational selection of syngeneic preclinical tumor models for immunotherapeutic drug discovery. Cancer Immunol Res 2017;5:29–41.

18. Lohse K, Kozlowski A, Strube MJ. Model specification in mixed-effects models: a focus on random effects. Commun Kinesiol 2023;1.

19. Razaghi A, Durand-Dubief M, Brusselaers N, Björnstedt M. Combining PD-1/PD-L1 blockade with type I interferon in cancer therapy. Front Immunol 2023; 14:1249330.

20. Adhit KK, Wanjari A, Menon S, K S. Liquid biopsy: an evolving paradigm for non-invasive disease diagnosis and monitoring in medicine. Cureus 2023;15: e50176.

21. Shegekar T, Vodithala S, Juganavar A. The emerging role of liquid biopsies in revolutionising cancer diagnosis and therapy. Cureus 2023;15:e43650.